

CrossMark  
click for updatesCite this: *Chem. Sci.*, 2015, 6, 1944

# A far-red emitting probe for unambiguous detection of mobile zinc in acidic vesicles and deep tissue†

Pablo Rivera-Fuentes,<sup>a</sup> Alexandra T. Wrobel,<sup>a</sup> Melissa L. Zastrow,<sup>a</sup> Mustafa Khan,<sup>b</sup> John Georgiou,<sup>b</sup> Thomas T. Luyben,<sup>bc</sup> John C. Roder,<sup>bc</sup> Kenichi Okamoto<sup>bc</sup> and Stephen J. Lippard<sup>\*a</sup>

Imaging mobile zinc in acidic environments remains challenging because most small-molecule optical probes display pH-dependent fluorescence. Here we report a reaction-based sensor that detects mobile zinc unambiguously at low pH. The sensor responds reversibly and with a large dynamic range to exogenously applied  $Zn^{2+}$  in lysosomes of HeLa cells, endogenous  $Zn^{2+}$  in insulin granules of MIN6 cells, and zinc-rich mossy fiber boutons in hippocampal tissue from mice. This long-wavelength probe is compatible with the green-fluorescent protein, enabling multicolor imaging, and facilitates visualization of mossy fiber boutons at depths of  $>100 \mu m$ , as demonstrated by studies in live tissue employing two-photon microscopy.

Received 4th November 2014

Accepted 2nd January 2015

DOI: 10.1039/c4sc03388d

www.rsc.org/chemicalscience

## Introduction

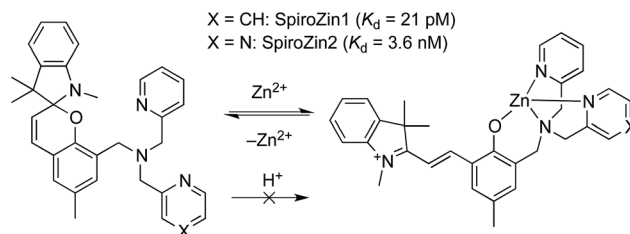
Zinc is an essential trace element that is often found as pools of mobile ions in specific tissues of the body.<sup>1</sup> In the brain and pancreas, the highest concentrations of mobile zinc occur in secretory vesicles.<sup>2–4</sup> Synaptic vesicles in neurons and insulin granules in pancreatic  $\beta$ -cells store zinc with concentrations in the millimolar range.<sup>5,6</sup> In both cases, these zinc ions are secreted together with either glutamate or insulin and elicit distinct autocrine and paracrine effects.<sup>4,7,8</sup>

Secretory vesicles are usually more acidic than the cytosol or the extracellular space. Insulin granules express an ATP-dependent proton pump that acidifies the vesicles to pH 5.5,<sup>9</sup> and the pH of resting synaptic vesicles in the hippocampus is 5.7.<sup>10</sup> Moreover, the acidity of secretory vesicles changes continuously, reaching neutrality upon exocytosis.<sup>10,11</sup> Visualization of vesicular zinc therefore requires probes that are completely impervious to pH changes.

The majority of small-molecule optical probes for mobile zinc comprise a fluorophore and a chelating unit.<sup>12–14</sup> In the

absence of zinc, lone pairs of tertiary amines in the binding unit quench the fluorescence of the fluorophore *via* photoinduced electron transfer (PET).<sup>15</sup> Upon zinc binding, the energy of the lone pair is decreased and PET becomes unfavorable, restoring the fluorescence of the probe. A limitation of this approach is that protonation of the tertiary amine in the binding unit also induces enhancement of the fluorescence. This pH sensitivity makes most zinc fluorescent sensors less efficient in acidic environments and may introduce uncertainty as to whether the observed signal is a consequence of detection of zinc or a change in pH.

We recently developed SpiroZin1, a reversible, reaction-based fluorescent sensor that is pH-insensitive from pH 3 to 7.<sup>16</sup> SpiroZin1 binds zinc with a dissociation constant in the picomolar range, which is too low for most neuroscience applications. Here we report the preparation of SpiroZin2 (Scheme 1), a probe that detects zinc with nanomolar affinity. The utility of



Scheme 1 Structure and sensing mechanism of SpiroZin probes. Replacement of a pyridine (X = CH) by a pyrazine ring (X = N) in the metal-chelating unit decreases the zinc binding affinity of the sensor, improving its dynamic range in live cells.<sup>17</sup>

<sup>a</sup>Department of Chemistry, Massachusetts Institute of Technology, Cambridge, MA 02139, USA. E-mail: lippard@mit.edu

<sup>b</sup>Lunenfeld-Tanenbaum Research Institute, Mount Sinai Hospital, Toronto, ON M5G 1X5, Canada

<sup>c</sup>Department of Molecular Genetics, Faculty of Medicine, University of Toronto, Toronto, ON M5S 1A8, Canada

† Electronic supplementary information (ESI) available: General methods, synthetic procedures, NMR spectra, kinetic data, pH profile, metal selectivity graph, cell culture and staining protocols, wide-field microscopy experiments, tissue specimen preparation, and two-photon imaging techniques. See DOI: 10.1039/c4sc03388d



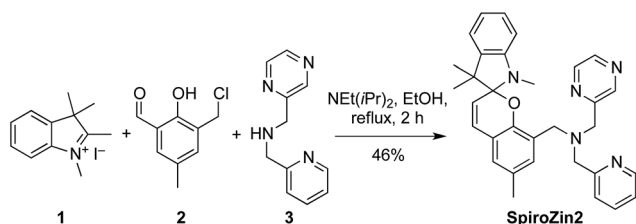
the probe is demonstrated in live cells and acute hippocampal tissue slices in studies that significantly enhance the value of the SpiroZin family of mobile zinc sensors.

## Results and discussion

SpiroZin2 was prepared in a one-pot reaction from indolenine 1, cresol derivative 2, and amine 3 (Scheme 2), and was purified by RP-HPLC (for details see the ESI†). Solutions of SpiroZin2 in aqueous buffer (50 mM PIPES, 100 mM KCl, pH 7) are pale yellow and non-fluorescent, indicating that the probe exists in the spirobenzopyran form. Addition of zinc turns the color of the solution to a deep red ( $\lambda_{\text{abs}} = 518 \text{ nm}$ ,  $3.071(1) \times 10^4 \text{ cm}^{-1} \text{ M}^{-1}$ ) with an increase in fluorescence intensity at  $\lambda_{\text{max}} = 645 \text{ nm}$  (Fig. S3†).

SpiroZin2 binds zinc with a dissociation constant of 3.6(4) nM. This affinity is weaker compared to that of SpiroZin1 as a consequence of replacing a pyridine ring by a less electron-rich, more weakly binding, pyrazine ring (Fig. S4†).<sup>18</sup> The fluorescence of the probe in the absence of zinc did not change significantly over the pH range of 3 to 7, and a large fluorescence enhancement was observed upon addition of zinc to solutions at each of these pH values (Fig. S5†). SpiroZin2 also displayed good selectivity against metal ions such as  $\text{Na}^+$ ,  $\text{K}^+$ ,  $\text{Ca}^{2+}$ , and  $\text{Mg}^{2+}$ , among others (Fig. S6†). The turn-on kinetics were studied using stopped-flow fluorescence spectroscopy and occurred in two steps, with  $t_{1/2 \text{ fast}} = 14.4(2) \text{ ms}$  and  $t_{1/2 \text{ slow}} = 2.92(5) \text{ s}$  (Fig. S7†). Upon chelation of zinc with ethylenediamine tetraacetic acid (EDTA), the non-fluorescent spirobenzopyran isomer was restored with  $t_{1/2} = 69.4(9) \text{ s}$  at  $37^\circ \text{C}$  (Fig. S8†).

The ability of SpiroZin2 to detect zinc ions in live cells was investigated. HeLa cells treated with  $5 \mu\text{M}$  SpiroZin2 showed essentially no fluorescence in the red channel (Fig. 1D). Addition of  $30 \mu\text{M}$  zinc pyrithione, a cell-permeable zinc complex, led to a 12-fold increase in intracellular red fluorescence (Fig. 1C and E). Treatment of these cells with the intracellular chelator  $N,N,N',N'$ -tetrakis(pyridin-2-ylmethyl)ethane-1,2-diamine (TPEN) decreased the fluorescence almost to background levels (Fig. 1C and F). In live HeLa cells, SpiroZin2 colocalizes with LysoTracker Green® (LTG), which is a commercial dye that stains acidic vesicles (Fig. 1G–I). The green and red signals correlate with a Pearson's correlation coefficient  $r_p = 0.80(2)$ . The Mander's colocalization coefficients<sup>19</sup> of the two signals are also close to 1 and the same for the two fluorescent signals ( $M_{\text{green}} = 0.8(1)$  and  $M_{\text{red}} = 0.8(1)$ ; for the mathematical definition of this coefficient see the ESI†),



Scheme 2 Synthesis of SpiroZin2.

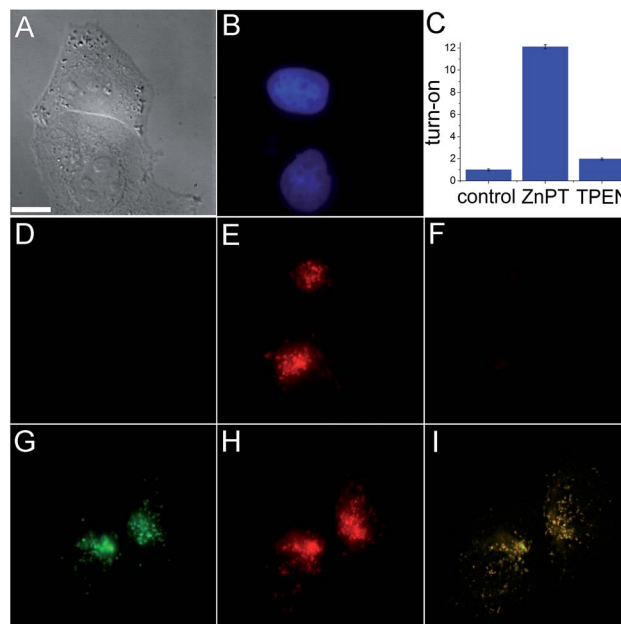


Fig. 1 Live HeLa cell imaging using SpiroZin2. (A) Differential interference contrast (DIC) image; (B) blue channel showing labeled nuclei; (C) quantification of the turn-on response; (D) red channel image of cells incubated with  $5 \mu\text{M}$  SpiroZin2; (E) red channel 10 min after treating the cells with  $30 \mu\text{M}$  ZnPT; (F) red channel 10 min after treating the cells with  $50 \mu\text{M}$  TPEN; (G) green channel showing HeLa cells treated with  $2 \mu\text{M}$  LTG; (H) red channel showing cells treated with  $5 \mu\text{M}$  SpiroZin2 and  $30 \mu\text{M}$  ZnPT; (I) overlay of deconvoluted images (G and H). Pearson's correlation coefficient:  $r_p = 0.80(2)$ . Images (A–F) and (G–I) correspond to two different plates. Scale bar =  $10 \mu\text{m}$ . ZnPT = zinc pyrithione; LTG = LysoTracker Green®.

indicating that SpiroZin2 detects exogenously applied zinc in acidic vesicles. To demonstrate that SpiroZin2 can also detect endogenous zinc in acidic environments, we used MIN6 cells, which are an insulinoma-derived model of pancreatic  $\beta$ -cells.<sup>20</sup>

Incubation of MIN6 cells with SpiroZin2 produced red fluorescence in a punctate pattern, especially in the vicinity of the plasma membrane (Fig. 2B and E), consistent with labeling of insulin granules.

Treatment of the cells with TPEN led to disappearance of the fluorescence signal, demonstrating that the sensor detects the presence of endogenous zinc (Fig. 2C). We loaded LTG and SpiroZin2 into MIN6 cells and quantified their colocalization. Whereas LTG stained all acidic vesicles, SpiroZin2 labeled only certain granules (Fig. 2D–F). The Pearson's correlation coefficient of the dyes in MIN6 cells is 0.66(4), which is significantly lower than that observed in HeLa cells (0.8). This smaller correlation coefficient is consistent with the ability of LTG to label both zinc-rich insulin granules and endo/lysosomes, in which the concentration of mobile zinc is low. In contrast, SpiroZin2 gives a fluorescent signal only in vesicles that have a high concentration of endogenous zinc, such as insulin granules, and leaves endo/lysosomes unstained (Fig. 2F). This conclusion is supported by the Mander's coefficients, which show that SpiroZin2 colocalizes strongly with LTG ( $M_{\text{red}} = 0.8(1)$ ), but LTG colocalizes with SpiroZin2 only moderately



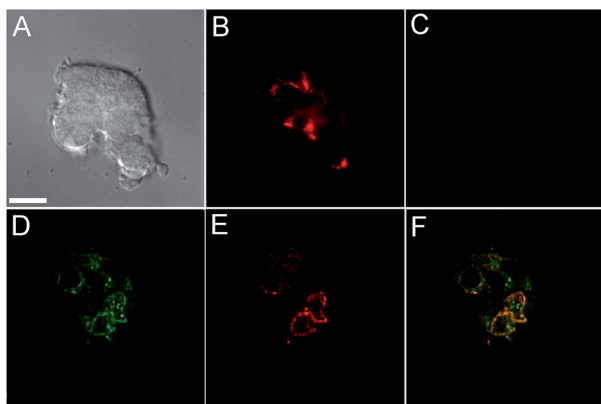


**Fig. 2** Live MIN6 cell imaging using SpiroZin2. (A) DIC image; (B) red channel showing cells treated with 5  $\mu\text{M}$  SpiroZin2; (C) red channel after treating the cells with 50  $\mu\text{M}$  TPEN; (D) deconvoluted green channel showing MIN6 cells treated with 2  $\mu\text{M}$  LTG; (E) deconvoluted red channel showing cells treated with 5  $\mu\text{M}$  SpiroZin2; (F) overlay of images (D) and (E). Pearson's correlation coefficient:  $r_p = 0.66(4)$ . Images (A–C) and (D–F) correspond to two different plates. Scale bar = 10  $\mu\text{m}$ .

( $M_{\text{green}} = 0.56(6)$ ). Additionally, the intracellular red fluorescence of MIN6 cells loaded with SpiroZin2 decreased significantly upon stimulation of the cells with 50 mM KCl and 20 mM glucose, which is consistent with exocytosis of vesicular zinc and SpiroZin2 (Fig. S9<sup>†</sup>).

SpiroZin2 displays a large fluorescence enhancement upon detection of zinc using two-photon excitation (Fig. S10<sup>†</sup>). Although the emission quantum yield of SpiroZin2 is very low ( $\phi = 0.001$ ), the relatively large two-photon absorption cross-section ( $\sigma_{\text{TPA}} = 74 \text{ GM}$ ) of the zinc-bound forms makes this sensor a good probe for two-photon imaging. We exploited these non-linear optical properties to perform two-photon imaging of live brain tissue. Acute hippocampal slices from adult wild-type (WT) mice were incubated with 100  $\mu\text{M}$  SpiroZin2. Two-photon imaging of these slices revealed red fluorescence with a punctate pattern in the cornu ammonis 3 (CA3) stratum lucidum layer in the mossy fiber region (Fig. 3A and C). This staining is similar to that obtained recently using probe 6-CO<sub>2</sub>H-ZAP4.<sup>21</sup> Vesicular zinc in the brain is loaded by the *ZnT3* (Slc30A3) transporter and this gene has been successfully knocked out in transgenic mice.<sup>22</sup>

Two-photon imaging of hippocampal tissue from a *ZnT3* knockout (*Slc30a3*<sup>-/-</sup>) mouse displayed only background fluorescence (Fig. 3B–D), demonstrating that SpiroZin2 detects *ZnT3*-dependent synaptic zinc in live tissue. The emission of SpiroZin2 in the deep red region of the spectrum enabled us to conduct zinc imaging experiments in Thy1-EGFP (line M) transgenic mice, which express EGFP sparsely in neuronal cells under the control of the Thy1 promoter.<sup>23</sup> Acute hippocampal slices of an adult Thy1-EGFP mouse were incubated with 100  $\mu\text{M}$  SpiroZin2 and imaged using two-photon microscopy (Fig. 4). In the green channel, neurons expressing EGFP can be observed in the dentate gyrus granule neurons and their mossy fiber axons (Fig. 4A). In the red channel, fluorescence is detected

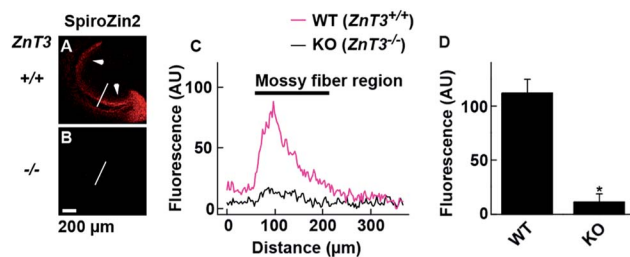


**Fig. 3** Visualization of vesicular zinc in hippocampal mossy fiber regions with SpiroZin2. (A and B) Representative images from adult WT *ZnT3* (+/+) mice (A) and *ZnT3* null (-/-) knockout (KO) mice (B). Slices were treated with 100  $\mu\text{M}$  SpiroZin2. Arrows indicate the mossy fiber region in the slice. (C) SpiroZin2 fluorescence profiles across the white line on the hippocampal images in (A) and (B). (D) Quantification of SpiroZin2 fluorescence intensity in the mossy fiber region of WT *ZnT3* (+/+) mice and *ZnT3* null (-/-) knockout (KO) mice. WT,  $n = 5$ ; KO,  $n = 5$ . \* $P < 0.001$ , unpaired  $t$  test. The peak at  $\sim 100 \mu\text{m}$  corresponds to the mossy fiber region. The background fluorescence intensity of the lines was adjusted to 0. Scale bar = 200  $\mu\text{m}$ .

in the mossy fiber boutons (Fig. 4B), but not in other regions including the cell bodies and dendrites of the dentate gyrus granule neurons (Fig. 4C). Enlarged images of the CA3 region reveal that SpiroZin2 produced a punctate staining pattern, which overlapped with EGFP-labeled mossy fiber boutons

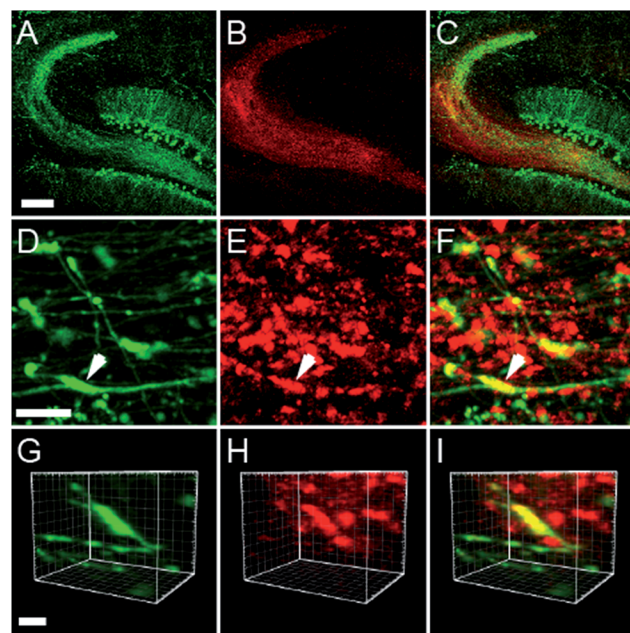


**Fig. 4** Acute hippocampal slices of adult mice (Thy1-EGFP, line M, transgenic mouse) stained with 100  $\mu\text{M}$  SpiroZin2. (A–C) Representative two-photon fluorescence images of the dentate gyrus and mossy fiber region in a hippocampal slice showing EGFP (A, green), SpiroZin2 (B, red), and the merged signal (C). Scale bar = 200  $\mu\text{m}$ . (D–F) Representative fluorescence images from presynaptic boutons in the mossy fiber layer from Thy1-EGFP hippocampal slice stained with SpiroZin2. EGFP fluorescence (D, green), SpiroZin2 (E, red) and the merged image (F). Scale bar = 10  $\mu\text{m}$ . (G–I) Enlarged, three-dimensional view of the colocalization of EGFP (green) and SpiroZin2 (red) in a mossy fiber bouton indicated by the arrow in D–F. Scale bar = 5  $\mu\text{m}$ .



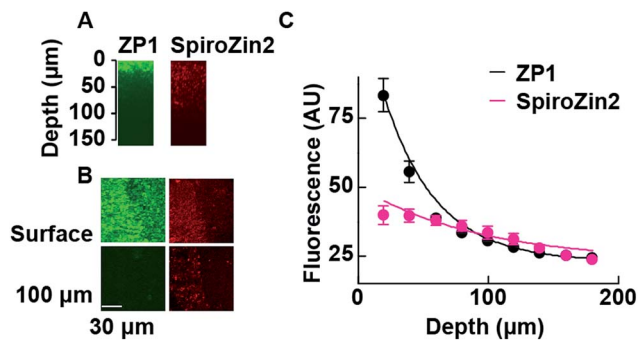


Fig. 5 Two-photon fluorescence profiles of ZP1 and SpiroZin2 along the z-axis of hippocampal tissues. (A) Representative x–z images of mossy fiber regions of acute hippocampal slices stained with ZP1 (green) and SpiroZin2 (red). Slices were stained with 25  $\mu\text{M}$  ZP1 and 100  $\mu\text{M}$  SpiroZin2 and imaged with constant laser power (860 nm, 10 mW). (B) Representative x–y images of mossy fiber region (left side of the images) on the slice surface (Surface) and at a 100–110  $\mu\text{m}$  depth (100  $\mu\text{m}$ ) stained with ZP1 (green) and SpiroZin2 (red). Scale bar = 30  $\mu\text{m}$ . (C) ZP1 and SpiroZin2 fluorescence profiles across the z-axis in the hippocampal tissues. The data were fit to a single exponential curve (ZP1:  $\tau = 40.3 \mu\text{m}$ , SpiroZin2:  $\tau = 94.0 \mu\text{m}$ ). ZP1,  $n = 3$ ; SpiroZin2,  $n = 3$ .

(Fig. 4D–F). Higher magnification of three-dimensional images confirmed the colocalized puncta of EGFP and SpiroZin2 (Fig. 4G–I), indicating presynaptic localization of SpiroZin2. Additionally, we co-stained hippocampal slices with SpiroZin2 and the membrane-permeable green fluorescent  $\text{Zn}^{2+}$  sensor ZP1, which was used previously to image mobile zinc in mossy fiber boutons.<sup>21</sup>

The fluorescent signals of SpiroZin2 and ZP1 correlate in the mossy fiber region and high-magnification images revealed colocalized puncta of SpiroZin2 and ZP1 (Fig. S11†). The addition of the membrane-permeant  $\text{Zn}^{2+}$  chelator tris-(2-pyridylmethyl)amine (TPA) reduced the fluorescence intensity of SpiroZin2 puncta, confirming the detection of presynaptic  $\text{Zn}^{2+}$ .<sup>21</sup> We next tested the decay of the detected fluorescence of zinc sensors as a function of depth ( $z$ ) in hippocampal tissues. We compared SpiroZin2 with ZP1.<sup>17</sup> The fluorescence intensity of ZP1 was more than twice as strong as that of SpiroZin2 on the surface of the tissue, but decayed dramatically to a fluorescence level similar to that of SpiroZin2, albeit showing increased out-of-focus fluorescence signals at deeper regions instead of distinct mossy fiber boutons (Fig. 5). In contrast, SpiroZin2 signals were dimmer at the surface, but maintained a fluorescence intensity consisting of focused presynaptic boutons at depths between 50–100  $\mu\text{m}$ . These results demonstrate the advantage of using SpiroZin2 to image  $\text{Zn}^{2+}$  in mossy fiber boutons from deep brain regions.

## Conclusions

We developed SpiroZin2, a probe with nanomolar binding affinity, pH-insensitivity in the physiological range, far-red fluorescence, and improved performance in live cells and tissues. This sensor accumulates in the endo/lysosomes of HeLa cells and displays a reversible 12-fold fluorescence

enhancement in response to exogenously applied  $\text{Zn}^{2+}$ . This experiment demonstrates that SpiroZin2 is able to detect chelatable zinc in acidic vesicles. In pancreatic MIN6 cells, SpiroZin2 labels zinc-rich granules and does not show fluorescence in other acidic vesicles. The emission of SpiroZin2 increases upon detection of zinc using two-photon excitation, making the probe useful for imaging in live tissue. SpiroZin2 stains the mossy fiber boutons in the CA3 region of WT mouse, but not in hippocampal slices of a *ZnT3* knockout (*Slc30a3*<sup>-/-</sup>) mouse, confirming that the probe detects presynaptic vesicular zinc. This sensor is also useful for experiments in combination with organisms that express EGFP reporters, providing the opportunity to study the interplay of mobile zinc and synaptic protein function by multicolor imaging. The far-red fluorescence of SpiroZin2 is ideal for imaging zinc in tissue at depths of >100  $\mu\text{m}$  with greater contrast than existing visible-light probes.

## Acknowledgements

This work was supported by the National Institute of General Medical Sciences [grant GM065519 (to S.J.L.)], the Natural Sciences and Engineering Research Council of Canada discovery Grants program (K.O.), Canadian Institutes of Health Research [grant MOP 111220 (to K.O.)], the Canada Research Chairs Program (K.O.), and the Canada Foundation for Innovation (K.O.). P. R.-F. thanks the Swiss National Science Foundation for a postdoctoral fellowship.

## Notes and references

- N. W. Solomons, *Ann. Nutr. Metab.*, 2013, **62**, 8–17.
- A. Takeda, M. Nakamura, H. Fujii and H. Tamano, *Metallomics*, 2013, **5**, 417–423.
- C. J. Frederickson, J.-Y. Koh and A. I. Bush, *Nat. Rev. Neurosci.*, 2005, **6**, 449–462.
- Y. V. Li, *Endocrine*, 2014, **45**, 178–189.
- C. J. Frederickson, S. W. Suh, D. Silva, C. J. Frederickson and R. B. Thompson, *J. Nutr.*, 2000, **130**, 1471S–1483S.
- M. C. Foster, R. D. Leapman, M. X. Li and I. Atwater, *Biophys. J.*, 1993, **64**, 525–532.
- K. Tóth, *Annu. Rev. Nutr.*, 2011, **31**, 139–153.
- S. L. Sensi, P. Paoletti, A. I. Bush and I. Sekler, *Nat. Rev. Neurosci.*, 2009, **10**, 780–791.
- J. C. Hutton, *Biochem. J.*, 1982, **204**, 171–178.
- G. Miesenböck, D. A. De Angelis and J. E. Rothman, *Nature*, 1998, **394**, 192–195.
- M. Ohara-Imaizumi, Y. Nakamichi, T. Tanaka, H. Katsuta, H. Ishida and S. Nagamatsu, *Biochem. J.*, 2002, **363**, 73–80.
- K. P. Carter, A. M. Young and A. E. Palmer, *Chem. Rev.*, 2014, **114**, 4564–4601.
- E. L. Que, D. W. Domaille and C. J. Chang, *Chem. Rev.*, 2008, **108**, 1517–1549.
- D. W. Domaille, E. L. Que and C. J. Chang, *Nat. Chem. Biol.*, 2008, **4**, 168–175.
- Z. Liu, W. He and Z. Guo, *Chem. Soc. Rev.*, 2013, **42**, 1568–1600.



- 16 P. Rivera-Fuentes and S. J. Lippard, *ChemMedChem*, 2014, **9**, 1238–1243.
- 17 S. C. Burdette, G. K. Walkup, B. Spingler, R. Y. Tsien and S. J. Lippard, *J. Am. Chem. Soc.*, 2001, **123**, 7831–7841.
- 18 X.-a. Zhang, D. Hayes, S. J. Smith, S. Friedle and S. J. Lippard, *J. Am. Chem. Soc.*, 2008, **130**, 15788–15789.
- 19 E. M. M. Manders, F. J. Verbeek and J. A. Aten, *J. Microsc.*, 1993, **169**, 375–382.
- 20 J.-I. Miyazaki, K. Araki, E. Yamato, H. Ikegami, T. Asano, Y. Shibasaki, Y. Oka and K.-I. Yamamura, *Endocrinology*, 1990, **127**, 126–132.
- 21 M. Khan, C. R. Goldsmith, Z. Huang, J. Georgiou, T. T. Luyben, J. C. Roder, S. J. Lippard and K. Okamoto, *Proc. Natl. Acad. Sci. U. S. A.*, 2014, **111**, 6786–6791.
- 22 T. B. Cole, H. J. Wenzel, K. E. Kafer, P. A. Schwartzkroin and R. D. Palmiter, *Proc. Natl. Acad. Sci. U. S. A.*, 1999, **96**, 1716–1721.
- 23 G. P. Feng, R. H. Mellor, M. Bernstein, C. Keller-Peck, Q. T. Nguyen, M. Wallace, J. M. Nerbonne, J. W. Lichtman and J. R. Sanes, *Neuron*, 2000, **28**, 41–51.

